Available online at www.sciencedirect.com
ScienceDirect

Biochimica et Biophysica Acta 1767 (2007) 404 – 413

Biochimica et Biophysica Acta
BBA
www.elsevier.com/locate/bbabio

Purification, crystallization and X-ray diffraction analyses of the *T. elongatus* PSII core dimer with strontium replacing calcium in the oxygen-evolving complex

Joanna Kargul [a], Karim Maghlaoui [a], James W. Murray [a], Zsuzsanna Deak [b], Alain Boussac [c], A. William Rutherford [c], Imre Vass [b], James Barber [a,*]

[a] *Wolfson Laboratories, Division of Molecular Biosciences, Faculty of Natural Sciences, Imperial College London, London, SW7 2AZ, UK*
[b] *Institute of Plant Biology, Biological Research Centre, Hungarian Academy of Sciences, H-6701 Szeged, Hungary*
[c] *Service de Bioénergétique, URA CNRS 2096, DBJC, CEA Saclay, 91191 Gif-sur-Yvette CEDEX, France*

Received 4 November 2006; received in revised form 5 January 2007; accepted 9 January 2007

Abstract

The core complex of photosystem II (PSII) was purified from thermophillic cyanobaterium *Thermosynechococcus elongatus* grown in Sr^{2+}-containing and Ca^{2+}-free medium. Functional in vivo incorporation of Sr^{2+} into the oxygen-evolving complex (OEC) was confirmed by EPR analysis of the isolated and highly purified SrPSII complex in agreement with the previous study of Boussac et al. [J. Biol. Chem. 279 (2004) 22809–22819]. Three-dimensional crystals of SrPSII complex were obtained which diffracted to 3.9 Å and belonged to the orthorhombic space group $P2_12_12_1$ with unit cell dimensions of $a = 133.6$ Å, $b = 236.6$ Å, $c = 307.8$ Å. Anomalous diffraction data collected at the Sr K-X-ray absorption edge identified a novel Sr^{2+}-binding site which, within the resolution of these data (6.5 Å), is consistent with the positioning of Ca^{2+} in the recent crystallographic models of PSII [Ferreira et al. Science 303 (2004) 1831–1838, Loll et al. Nature 438 (2005) 1040–1044]. Fluorescence measurements on SrPSII crystals confirmed that crystallized SrPSII was active in transferring electrons from the OEC to the acceptor site of the reaction centre. However, SrPSII showed altered functional properties of its modified OEC in comparison with that of the CaPSII counterpart: slowdown of the Q_A-to-Q_B electron transfer and stabilized $S_2Q_A^-$ charge recombination.

Keywords: Photosynthesis; Photosystem II structure; Strontium replacement; X-ray crystallography; Fluorescence decay and imaging; Water splitting

1. Introduction

The light-driven water splitting reaction of photosynthesis occurs in Photosystem II (PSII), a multisubunit membrane protein complex embedded in the thylakoid membranes of plants, algae and cyanobacteria [1]. In so doing it produces dioxygen and reducing equivalents, where the latter enter the photosynthetic electron transfer chain destined ultimately, with the input of additional energy from Photosystem I (PSI), to convert carbon dioxide to organic molecules. The catalytic site that forms the oxygen evolving centre (OEC) contains a cluster of four manganese ions that act to accumulate oxidizing equivalents required to produce a dioxygen molecule from two substrate water molecules as formulated in the S-state cycle [2,3]. It has been known for some time that a single tight-binding Ca^{2+} ion is essential for this cycle to function and oxygen to be released [4–7]. This cation is also required for the assembly of the Mn-cluster during photoactivation of oxygen evolution [8–10]. Evidence that

---

Abbreviations: PSI and II, photosystem I and II; OEC, oxygen-evolving complex; PQ, plastoquinone; Chl, chlorophyll; EPR, electron paramagnetic resonance; ICP, inductively coupled plasma optical emission spectrometry; EXAFS, extended X-ray absorption fine structure; FT-IR, Fourier transform infrared; MAD, Multiple-wavelength Anomalous Diffraction; HIC, hydrophobic interaction chromatography; AEC, anion-exchange chromatography; MES, 2-(N-morpholino)ethanesulfonic acid; DCMU, 3-(3,4-dichloropheny1)-1,l-dimethylurea; DDM, dodecyl-β-D-maltoside; DMSO, dimethyl sulphoxide

[*] Corresponding author. Tel.: +44 20 759 45266; fax: +44 20 759 45267.
E-mail address: j.barber@imperial.ac.uk (J. Barber).

0005-2728/$ - see front matter. Crown Copyright © 2007 Published by Elsevier B.V. All rights reserved.
doi:10.1016/j.bbabio.2007.01.007

Ca^{2+} is closely associated with the Mn-cluster comes from a range of different studies, including extended X-ray absorption fine structure (EXAFS) [11–14], electron paramagnetic resonance (EPR) [4,15,16] and recently, X-ray diffraction analyses [17,18].

In the case of X-ray diffraction analyses Mn ions and Ca^{2+} are not distinguishable in a standard electron density map produced from a crystallographic X-ray diffraction experiment. Furthermore, at the resolutions used to produce the current structures [17,18] it is not possible to resolve the individual metal ions. For this reason the two crystal structures of PSII have slightly different conformations of the metal atoms of the OEC. Until atomic resolution diffraction is available for PSII, special techniques must be employed to help resolve the positioning of metal ions as emphasized by application of EXAFS [13,14,19] and by collecting anomalous X-ray diffraction data [17,18]. An anomalous difference map using model-derived phases is a very sensitive way to locate anomalous scatterers in a protein crystal as demonstrated by the identification of a Ca^{2+} ion bound to the PsbO protein of PSII [20]. However in general, using a single wavelength, it is impossible to unambiguously identify metal ions by element, as the height of the peak may vary due to occupancy and dynamic and static disorder. If datasets are collected at a small energy shift above and below an elemental X-ray absorption edge, there will be a much larger signal coming from the metal atom site above the edge than below it. These datasets can be subtracted in reciprocal space [21] to produce a double-difference anomalous Fourier map. Peaks in this map correspond to the element of interest as the contributions of all other elements cancel nearly completely in the calculation and so are negligible. Surprisingly, this very powerful technique seems to be rarely reported in the literature.

We have collected such data and calculated maps for PSII at the Mn K-edge (6.539 keV, 1.896 Å), as reported in Ferreira et al. [17]. However, the Ca K-edge is at 4.03 keV (3.07 Å), and therefore it is very difficult to collect diffraction data at such a low energy due to the strong X-ray absorption at this wavelength. In contrast, the Sr K-edge is at 16.1 keV (0.7699 Å), which is accessible by tunable synchrotron beamlines used for anomalous dispersion experiments. The anomalous signal at this energy is nearly four electrons, so the site should be detectable even at low Sr^{2+} occupancy. Since Sr^{2+} can functionally replace Ca^{2+} in the OEC site, we have prepared PSII crystals with Ca^{2+} substituted by Sr^{2+}, collected diffraction data above and below the Sr K-edge and calculated double difference anomalous Fourier maps. The replacement of Ca^{2+} in the OEC by Sr^{2+} was achieved by growing the cyanobacterium *Thermosynechococcus elongatus* in a Ca^{2+}-free, Sr^{2+}-containing medium. It has been shown that full Sr^{2+} occupancy of the OEC is achieved by this biosynthetic incorporation and that the catalytic activity is fully maintained as compared with biochemical replacement of Ca^{2+} by Sr^{2+} using isolated PSII [11], a factor which was critical for growing ordered 3D crystals. The main effect of the alkali metal exchange induced biosynthetically is to slow the S_3-to-S_0 transition, and therefore reduce the oxygen evolution rate [11].

2. Materials and methods

2.1. Culturing of cells

Thermosynechococcus elongatus (BP-1 strain) cells were grown as 20 l cultures at 45 °C under continuous white light illumination and gradually increasing light intensity of 50–120 μmol photons m^{-2} s^{-1}. The cells were grown in a Ca^{2+}-free Sr^{2+}-containing DTN medium [22] with 0.8 mM $SrCl_2$ and aerated with 2% CO_2-enriched air [11]. Cells were grown to late log phase until an OD_{685} of 1.2 was reached. The residual Ca^{2+} content in the Sr^{2+}-DTN medium was negligible (1.29 μM as determined by inductively coupled plasma optical emission spectrometry (ICP)), similar to that reported by Boussac et al. [11]. The culturing of *T. elongatus* in Ca^{2+}-rich medium was performed as in Ferreira et al. [17].

2.2. Preparation of thylakoids

Thylakoid membranes were purified according to a modified method described in [11]. Briefly, cells from 20l cultures were concentrated 10-fold using tangential flow cell concentrator (Sartorius Sartocon, Millipore). Concentrated cells were harvested by centrifugation at 10,000 rpm for 10 min. (JA14 rotor, Beckmann), washed in buffer 1 (40 mM MES pH 6.5, 15 mM, $MgCl_2$, 15 mM $CaCl_2$, 10% glycerol, 1.2 M betaine) and resuspended in the same buffer containing 0.2% (w/v) BSA, 1 mM benzamidine, 1 mM aminocaproic acid, 1 mM Pefabloc and 50 μg/ml DNAse I and RNAse. The cells were broken by passing through a French Press (≈6000 psi) twice. Unbroken cells were removed by centrifugation (1000×*g*, 2 min). Thylakoids were pelleted by centrifugation at 180,000×*g* for 20 min at 4 °C and washed twice with buffer 1. Resultant thylakoid pellets were resuspended in buffer 1 at a chlorophyll (Chl) concentration of 1 mg/ml, snap-frozen in liquid N_2 and stored at −70 °C prior to use.

2.3. Isolation of PSII core dimers

Sr^{2+}-containing thylakoids were solubilised with 1.2% dodecyl-β-D-maltoside (DDM) (w/v) (Biomol) and 0.5% sodium cholate (w/v) (Sigma) at a Chl concentration of 1 mg/ml for 30 min at room temperature in the dark. Solubilisation of Ca^{2+}-containing thylakoids was performed as in [18]. The isolation and purification of SrPSII and CaPSII core dimers was performed essentially as in [17] using hydrophobic interaction chromatography (HIC) followed by anion-exchange chromatography (AEC), in the presence or absence of 1M betaine during all purification steps. All the chromatographic media and columns were applied according to Ferreira et al. [17]. The flow rates were 5 ml/min or 7.5 ml/min for the HIC in the presence or absence of 1 M betaine, respectively. For the AEC, flow rates of 1 ml/min or 4 ml/min were applied in the presence or absence of 1 M betaine, respectively. The fractions were analysed by absorbance spectroscopy and size exclusion chromatography as in [17]. The PSII core samples were washed using Centricon YM-100 (Amicon) concentrating devices with 4 ml of 20 mM MES pH 6.5, 10 mM $CaCl_2$ and 10 mM $MgCl_2$ in the presence or absence of 1 M betaine, and finally concentrated in the same buffer to 1.75 mg Chl/ml using Centricon YM-100 concentrators (Amicon). The PSII monomer:dimer ratio was determined by analytical size exclusion chromatography as in [17]. The oxygen-evolving activity of the purified SrPSII cores was monitored using a Clark electrode (Hansatech) as previously described by Boussac et al. [11].

2.4. SDS-PAGE of PSII core complexes

SDS-PAGE was carried out using the Tris-Tricine system described by Schägger and von Jagow [23]. Protein bands were resolved on 12.5% polyacrylamide gels in the presence of 6 M urea and visualized with Coomassie brilliant blue R-250 using standard procedures. Prestained protein size markers (low-range, Bio-Rad) were used for estimation of apparent size of PSII components.

2.5. Crystallization of CaPSII and SrPSII

Both SrPSII and CaPSII crystals were grown at 17 °C using the hanging drop vapour diffusion method in the presence of 5–8% PEG-4000 (Fluka), 0.5 mM of methyl mercurial chloride (Hampton Research) and 0.055 mM polyoxyethylene lauryl ether ($C_{12}E_8$) (Hampton Research), as described in [17]. Crystals were cryoprotected in 25% glycerol added stepwise as described in [17] and frozen in liquid nitrogen. Microscopic images of the crystals were acquired with SZX-12 Olympus Stereomicroscope coupled to a DP12 digital camera.

2.6. Continuous Wave-EPR Measurements

CW-EPR spectra were recorded using a standard ER 4102 (Bruker) X-band resonator with a Bruker ESP300 X-band spectrometer equipped with an Oxford Instruments cryostat (ESR 900). Flash illumination at room temperature was provided by a Nd:YAG laser (532 nm, 550 mJ, 8 ns Spectra Physics GCR-230-10). For measurements of the S_2-multiline signal, PSII samples were loaded into quartz EPR tubes in the dark and further dark-adapted for 1 h at room temperature. The PSII samples were then synchronized in the S_1-state with one pre-flash. After another dark period of 1 h at room temperature, 1 mM phenyl-p-benzoquinone dissolved in DMSO was added (final concentration of DMSO was less than 3%). Immediately after flash illumination, given at room temperature, the samples were frozen at 198 K (ethanol and dry ice bath) in the dark. Then the samples were transferred to liquid nitrogen before being inserted into the EPR cryostat. Instrument settings were: temperature, 8.5 K; modulation amplitude, 25 gauss; microwave power, 20 mW; microwave frequency, 9.4 GHz; modulation frequency, 100 kHz. The central parts of the spectra corresponding to the TyrD· region were deleted.

2.7. Flash-induced fluorescence decay measurement

Flash-induced increase and subsequent decay of chlorophyll fluorescence yield was measured by a double-modulation fluorometer (Photon Systems Instruments, Brno), in the 150 µs–100 s time range. Core particles concentration was 10 µg of Chl/ml in a normal 10 × 10 mm cuvette. PSII crystals were measured in a custom-made plexiglass holder of 10 µl sample volume containing 10–30 crystals and closed with a cover slip. Samples were illuminated with orange measuring light pulses of 2.5 µs and red actinic light flashes of 20 µs. In order to increase the very low signal intensity of the crystals, optical properties of the equipment were improved by applying lenses and a mirror around the sample holder. Data processing and deconvolution of the relaxation curves was performed as in [24].

2.8. Fluorescence imaging of crystals

Room-temperature chlorophyll fluorescence images of the crystals were taken after 3 min of dark adaptation at the 25× magnification using the special saturation pulse routine provided by ImagingWin™ software (Walz, Germany). The microscopy-version of the Imaging-PAM was employed based on the H600AFL Epifluorescence Microscope (Hund, Wetzlar) connected to a Multi Control Unit IMAG-CM of the Imaging-PAM M-series fluorometer (Walz, Germany). The fluorescence was recorded by the IMAG-MAX/K CCD camera. A single high-power Luxeon LED (450 nm) was employed for measuring light pulses as well as for actinic illumination and saturation pulses. For the quantification of apparent F_0' and F_m values, the Micro-version of the same Imaging-PAM fluorometer was used to minimize the actinic effect of measuring light pulses under the microscope. The value of the true F_0 (dark-adapted fluorescence level) was not attainable in these experiments due to the photochemically-induced effects of the weak background measuring light.

2.9. X-ray data collection and analysis

X-ray data sets were collected using the undulator Multiple-wavelength Anomalous Diffraction (MAD) beamline X06SA at the Swiss Light Source. Data were collected from a Sr^{2+}-substituted PSII crystal which diffracted to 3.9 Å. Two datasets were collected from different regions of the same crystal, above and below the Sr K-edge, dubbed HER and LER. Each dataset consisted of a full 360° degree sweep of the single-axis goniometer. The HER dataset was collected with 16.150 keV radiation and the LER with 16.089 keV radiation. The datasets were integrated with MOSFLM [25] and scaled together with SCALA [26]. The recent 3.0 Å model (2AXT.pdb), with the metal atoms of the OEC removed was used as a molecular replacement model in PHASER [27] then subjected to rigid-body refinement in REFMAC5 [28]. The model phases and figures-of-merit were then used to calculated anomalous difference Fourier maps for the HER and LER datasets according to the following formula derived by [21]:

$$\rho_{\mathrm{DDANOxyz}} = \sum_{\mathrm{hkl}} W\left(\left(|F^{+}_{\mathrm{HER}}| - |F^{-}_{\mathrm{HER}}|\right) - \left(|F^{+}_{\mathrm{LER}}| - |F^{-}_{\mathrm{LER}}|\right)\right) \times \exp\left(-2\pi i(\mathrm{hx} + \mathrm{ky} + \mathrm{lz}) + i\left(\alpha - \frac{\pi}{2}\right)\right)$$

A "double-difference anomalous Fourier" (DDANO) map, similar to that described by Than et al. [21], was calculated from the HER and LER datasets and model phases using programs of the CCP4 suite [29]. All of these maps were then subjected to 2-fold averaging between the two crystallographically independent monomers in the crystal with the MAPROT program [30] using a mask of radius 3 Å around the monomer. Figures were produced using the PYMOL program [31]. Structures were superimposed and averaging operators were obtained from the SSM function [32] of the COOT program [33] using the D1 protein amino acid chain of the models as a reference.

3. Results

3.1. In vivo incorporation of strontium into the oxygen involving complex of photosystem II

Strontium is the only divalent cation that replaces calcium in the OEC whilst maintaining activity of the water-splitting and oxygen evolution [4,34,35]. We have obtained highly pure PSII core preparations from cells of the thermophillic cyanobacterium *T. elongatus* grown in the Ca^{2+}-free and Sr^{2+}-rich medium. Under these conditions the cells incorporated Sr^{2+} in place of Ca^{2+} into the OEC of the PSII as reported by Boussac et al. [11] and verified by EPR measurements (see below). Two populations of highly pure SrPSII complexes were obtained through two-step chromatographic separation of PSII dimers in the presence or absence of betaine, a compound previously reported to ensure full occupancy of Sr^{2+} in the OEC of PSII [11]. Fig. 1A shows a typical elution profile of the hydrophobic interaction chromatography step in the presence of 1 M betaine, where PSII is present in the second elution peak preceded by carotenoids and followed by the phycobilisome and photosystem I (PSI) fractions. Fig. 1B represents a chromatogram of the subsequent anion-exchange chromatography purification step with the PSII monomer eluting first followed by the major PSII dimer peak. Similar elution profiles were obtained for the fractions purified in the absence of betaine (data not shown) and were consistent with those reported previously [17,36]. The PSII monomer: dimer ratio was typically 1:5 as determined by analytical size exclusion chromatography (see Fig. 1C), although it was as low as 1:9 in several best preparations. SDS-PAGE analysis provided a protein profile of dimeric SrPSII protein confirming that all extrinsic subunits, in particular the 33 kDa (PsbO), 12 kDa (PsbU) and cytochrome *c*-550 (PsbV) proteins, remained intact in both plus-and-minus-betaine-treated SrPSII preparations (see Fig. 1D). The average oxygen evolving activities of SrPSII dimer preparations (16 independent preparations) varied between 1300 µmol O_2 mg Chl^{-1} h^{-1} and 1700 µmol O_2 mg Chl^{-1} h^{-1}, and were typically 25% higher for the SrPSII dimer samples purified in the absence of betaine. Although the maximum oxygen rates are lower in

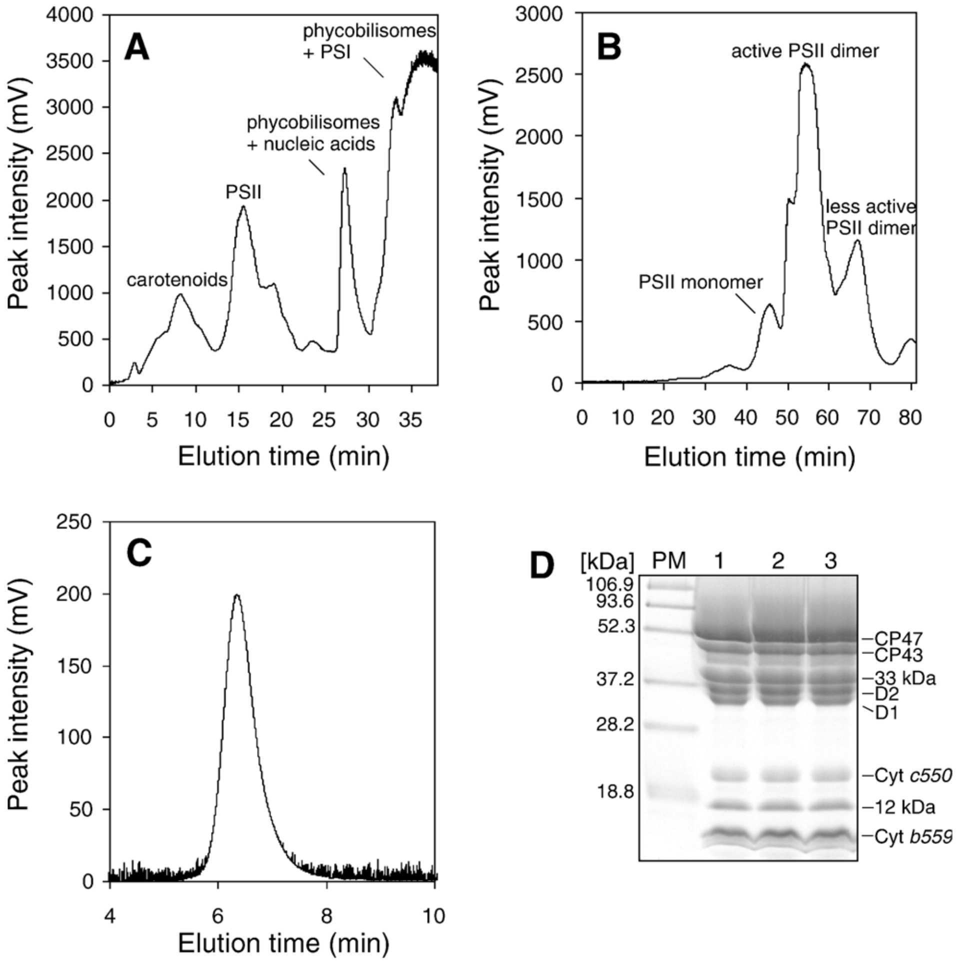

Fig. 1. Purification of SrPSII core dimers in the presence of betaine. Chromatograms from the hydrophobic interaction (HIC) (A) and anion-exchange (AEC) (B) chromatography steps in the presence of 1 M betaine. The POROS ET (Applied Biosystems) and UNO Q-12 (Bio-Rad) columns were employed for the HIC and AEC steps, respectively. Bed volumes were 44 ml and 12 ml, respectively. Flow rates were 5 and 1 ml/min, respectively. (C) Analytical size-exclusion HPLC of purified SrPSII crystallization sample. (D) Protein composition of purified SrPSII core dimers. PM, prestained protein markers with their apparent M_{wt} (kDa) indicated on the left; lane 1, CaPSII dimer; lane 2, SrPSII dimer purified in the presence of 1 M betaine; lane 3, SrPSII dimer purified in the absence of betaine. Proteins were separated on SDS-PAGE at 5 μg of Chl/lane.

SrPSII than in CaPSII when the Ca^{2+} has been substituted by Sr^{2+} biosynthetically, the difference is not due to the presence of inactive sites but rather to a modification of S-state cycle kinetics (see below and Ref. [11]).

We have estimated Sr^{2+} occupancy in the OEC in both types of SrPSII dimer samples (purified in the presence or absence of betaine) using EPR spectroscopy. Fig. 2 shows the EPR spectra recorded at liquid helium temperature from SrPSII dimer samples (spectra 1–6) compared to a typical multiline signal for CaPSII preparations (spectrum 7). Spectrum 1 was recorded from the SrPSII core sample purified in the absence of betaine and pre-adapted in the dark for 1 h to obtain synchronized S_1-redox state centres. Spectrum 2 was recorded following exposure to a single light flash at room temperature when most centres are converted to their S_2-state. Spectrum 3 represents the difference spectrum between light and dark spectra obtained from SrPSII purified in the absence of betaine. This S_2 multiline signal is clearly different from a normal S_2-multiline signal from CaPSII (see spectrum 7) and partly exhibits the characteristic pattern observed for in vitro Sr^{2+}-reconstituted PSII [37] and in vivo generated SrPSII [11]. However, contribution of Ca^{2+}-containing OEC centres is apparent in this SrPSII sample and most likely reflects partial exchange of Sr^{2+} for Ca^{2+} in the OEC of SrPSII purified in the absence of betaine. Spectrum 4 is the contribution of Sr^{2+}-containing PSII in spectrum 3 and spectrum 5 is the contribution of Ca^{2+}-containing PSII in spectrum 3. Spectrum 6 in Fig. 2 represents a typical S_2-multiline recorded for the SrPSII dimer purified in the presence of betaine which clearly corresponds to 100% Sr^{2+} occupancy in the OEC of this type of SrPSII sample. This S_2-multiline signal (between 2500 and 4300 gauss) is similar to that previously observed by Boussac et al. [11]. Spectrum 7 is a multiline for CaPSII which was recorded from PSII purified in the presence of betaine and obtained from cells grown in the presence Ca^{2+} as described by Boussac et al. [11]. The relative proportion of Sr^{2+} occupancy in the OEC from SrPSII purified in the absence of betaine was estimated as 50% ± 10% following interactive subtraction of spectra 6 and 7 from spectrum 3.

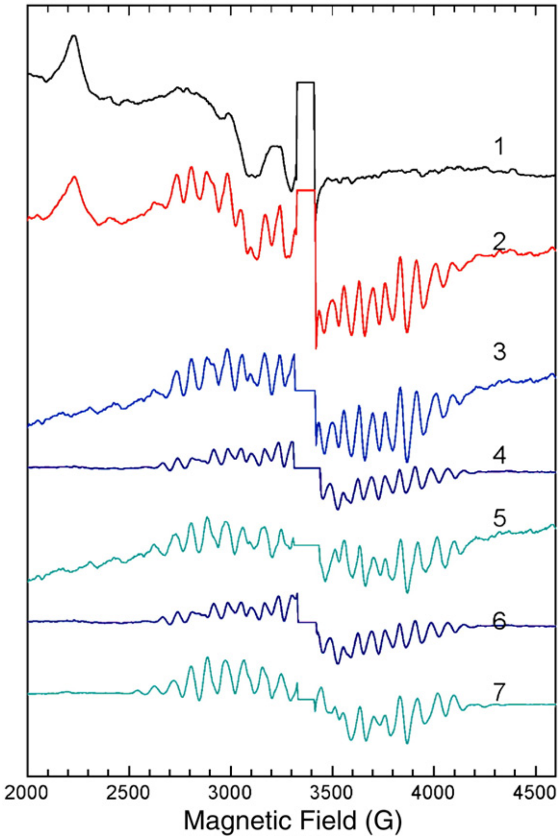

Fig. 2. Estimation of Sr^{2+} occupancy in the OEC of purified SrPSII core dimers by EPR. Continuous Wave-EPR spectra were recorded using conditions described in Materials and methods. Spectrum 1 (black) was recorded from the dark-adapted SrPSII core sample. Spectrum 2 (red) was recorded after 1 flash given at room temperature. Spectrum 3 (blue) is light-minus-dark. Spectrum 6 (dark blue) is a typical Sr-multiline and spectrum 7 (dark cyan) is a typical Ca-multiline. The latter two spectra were recorded from PSII purified in the presence of 1 M betaine from cells grown either in the presence of Sr^{2+} or Ca^{2+}, respectively. Spectrum 4 is the contribution of Sr^{2+}-containing PSII in spectrum 3 and spectrum 5 is the contribution of Ca^{2+}-containing PSII in spectrum 3.

3.2. Three-dimensional crystallization of SrPSII

Both types of highly pure and homogeneous SrPSII dimer samples (obtained in the presence or absence of betaine) were successfully used for obtaining 3D crystals. The crystals were grown with PEG-4000 as the precipitant and in the presence of a secondary detergent $C_{12}E_8$ and a mercury derivative to improve the crystal size and diffracting quality. The best diffracting and the largest crystals were obtained from the SrPSII samples purified in the absence of betaine and therefore containing 50% Sr^{2+} in the OEC as described above. Their typical shape and size are shown in Fig. 3. The best crystals diffracted to 3.9 Å and belonged to the orthorhombic space group $P2_12_12_1$ with unit cell dimensions of a = 133.6 Å, b = 236.6 Å, c = 307.8 Å (see Suppl. Table S1). For functional comparative studies, both types of SrPSII crystals (with 100% and 50% Sr^{2+} occupancy in the OEC) were analysed, whereas for X-ray diffraction data acquisition only crystals obtained from the SrPSII core sample purified in the absence of betaine were used since they provided better quality data.

3.3. Functional characterization of SrPSII cores and crystals

The purified SrPSII cores with 50% or 100% Sr^{2+} occupancy in the OEC and the resultant crystals were shown to be active in electron transfer from the OEC to Q_A and Q_B as monitored by fluorescence imaging of the crystals (Fig. 4) and by flash-induced fluorescence decay measurements on SrPSII cores and crystals (Fig. 5). As seen in Fig. 4, the fluorescence of the dark-adapted crystals subjected to weak measuring light increased from an apparent minimal level F_0' from PSII centres containing oxidized Q_A to maximum fluorescence F_m (reflecting reduction of Q_A) upon actinic light illumination. The $F_v/F_m = (F_m - F_0')/F_m$ variable fluorescence ratio gives the quantum yield of PSII for Q_A reduction, and provides a relative measure of functional activities of native CaPSII and SrPSII crystals (see Table 1). The F_v/F_m ratio was smaller in SrPSII crystals in comparison to CaPSII crystals (85% and 75% with 50% and 100% Sr^{2+} occupancy in the OEC, respectively). This indicates a lower quantum yield of PSII in the SrPSII crystals, which is most likely related to somewhat decreased efficiency of electron donation from the Mn cluster to Q_A. It is of note that the measuring light, which is required to obtain good signal-to-noise ratio of the very weak fluorescence measured from the

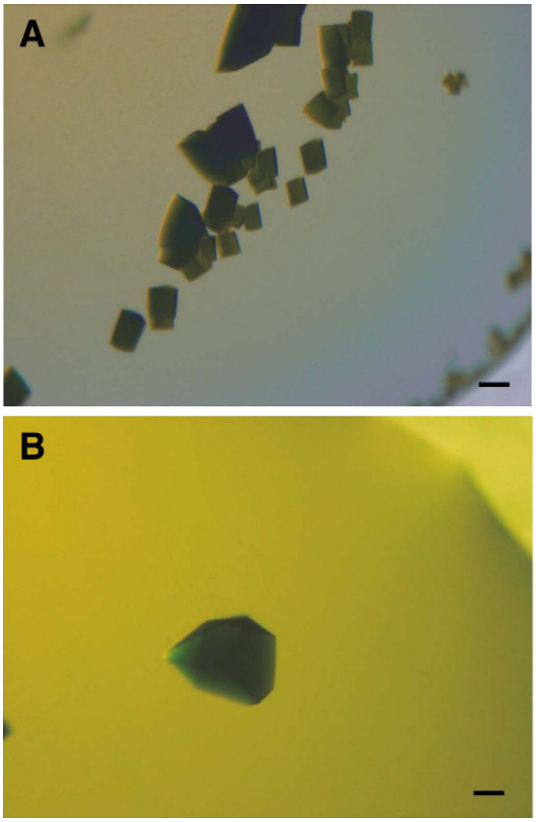

Fig. 3. Light microscopic images of three-dimensional SrPSII crystals. The crystals were grown by the hanging-drop vapour diffusion method for 3 days in the presence of PEG-4000 as a precipitant (see Materials and methods). They were typically 200 μm × 300 μm × 50 μm in size. (A) A typical set of SrPSII crystals from the core sample purified in the absence of betaine. (B) Enlarged image of a single SrPSII crystal obtained in the absence of betaine. Scale bars correspond to 100 and 50 μm in A and B, respectively.

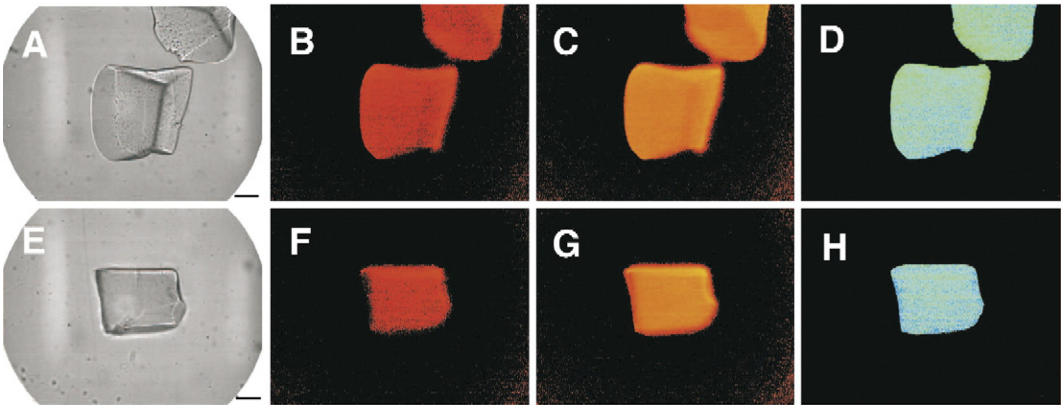

Fig. 4. Fluorescence imaging of SrPSII (A–D) and CaPSII (E–H) crystals. A, E, light microscopic images of crystals at 25× magnification; B, F, corresponding F_0' fluorescence images; C, G, F_m maximum fluorescence images; D, H, F_v/F_m images. Scale bars in A and E represent 50 μm. Fluorescence images are shown with artificial colour coding in which the fluorescence intensity increases from red to blue. Chlorophyll fluorescence images were obtained as described in Materials and methods.

small amount PSII centres in the crystals induces some actinic effect, which decreases the variable fluorescence values. Even though we used a non-microscopic version of the fluorescence imager, in which the actinic effect of the measuring light is smaller than in the microscopic version, to quantify variable fluorescence from the crystals some actinic effect on the F_0 level might still be present. However, this affects the different samples to the same extent and does not influence the relative change of variable fluorescence among the different samples.

Illumination of isolated cores with a single-turnover saturating flash induces the reduction of Q_A by an electron extracted from the Mn cluster, which leads to increased fluorescence yield. Subsequent reoxidation of Q_A^- in the dark results in the relaxation of fluorescence yield exhibiting three main decay phases [38–40], as shown in Fig. 5. The fast phase, which contributes to ≈50% of the total decay with 1.5 ms half time in CaPSII cores arises from the reoxidation of Q_A^- by plastoquinone (PQ) molecules bound to the Q_B site before the flash. This phase was somewhat slowed down (1.7 and 2.0 ms in the 50% and 100% Sr^{2+} occupancy in the SrPII cores, respectively), concomitant with the decrease of their relative amplitudes (40% and 25%, respectively). The middle phase (90 ms half time and 15% relative amplitude in CaPSII) originates from Q_A^- reoxidation by PQ molecules in centres where the Q_B site was empty at the time of the flash. This phase was slightly slowed down in the 100% Sr^{2+} occupancy SrPSII cores (100 ms), but the relative amplitude was unchanged. The middle phase is significantly slower than in thylakoids of *T. elongatus* (18–20 ms, not shown). This component is assigned to PQ binding to the Q_B site after the flash, which is most likely a second order process whose rate depends linearly on the concentration of available oxidized PQ. Thus, the significantly slower slow phase in the core particles as compared to thylakoids most likely reflects the largely decreased PQ pool size in the core complexes. Finally, the slow phase (11 s half time and 35% relative amplitude in the CaPSII cores) arises from back reaction of the S_2 state of the water-oxidizing complex with Q_A^-, which is populated via the equilibrium between $Q_A^-Q_B$ and $Q_AQ_B^-$. This phase became faster in the SrPSII cores (9.8 and 9.6 s in the 50% and 100% Sr^{2+} occupancy samples, respectively) concomitant with the increase of its relative amplitude (44% and 59% in the 50% and 100% Sr^{2+} occupancy samples, respectively).

DCMU, a well-known inhibitor of Q_A to Q_B electron transfer [41], eliminated the fast and middle phases, and fluorescence decayed predominantly in the slow (≈8 s) phase representing the recombination of the $S_2Q_A^-$ state [24,42,43]. The fluorescence decay kinetic was somewhat slower in the SrPSII cores (9.9 and 9.5 s in the 50% and 100% Sr^{2+} occupancy samples, respectively) showing the stabilization of $S_2Q_A^-$ recombination as a consequence of replacing Ca^{2+} with Sr^{2+} (see Fig. 5). The practically identical decay time of the slow phase in the absence and presence of DCMU indicates that the redox potentials of Q_A and Q_B are very similar in the SrPSII samples. This is in agreement with the increased relative amplitude of the slow phase, which reflects the equilibrium constant for sharing the electron between $Q_A^-Q_B$ and $Q_AQ_B^-$ [39].

Flash-induced chlorophyll fluorescence signals are also observed in the SrPSII crystals (see Fig. 5). The initial part of the curve is disturbed by a measuring artefact, which is also present in empty sample holder under the same high sensitivity measuring conditions, thus the 1st reliable point is at 500 μs after flash. Although the quality of the data does not permit reliable resolution of the fast and middle decay phases, a fast decaying fluorescence component is clearly present in the absence of DCMU demonstrating forward electron transfer from Q_A^- to Q_B in the SrPSII crystals. The kinetics of the slow phase is very similar to that of the SrPSII cores (about 11 s half time and 54% relative amplitude). In the presence of DCMU, the decay is dominated by a slow phase with 11 s halftime in the SrPSII crystals, which is very similar to that obtained in the respective core particles, demonstrating that the inhibitor has accessed the Q_B site in the crystallized PSII. The half time of the slow phase in the SrPSII crystals is about 15 s in contrast to the 9–10 s half time obtained in the core particles from which the crystals were grown. This indicates that some stabilization of the $S_2Q_A^-$ charge-separated state occurs when PSII centres are packed into the crystal lattice. These data provide a proof for light-induced charge stabilization in the $S_2Q_A^-$ state in SrPSII crystals and also

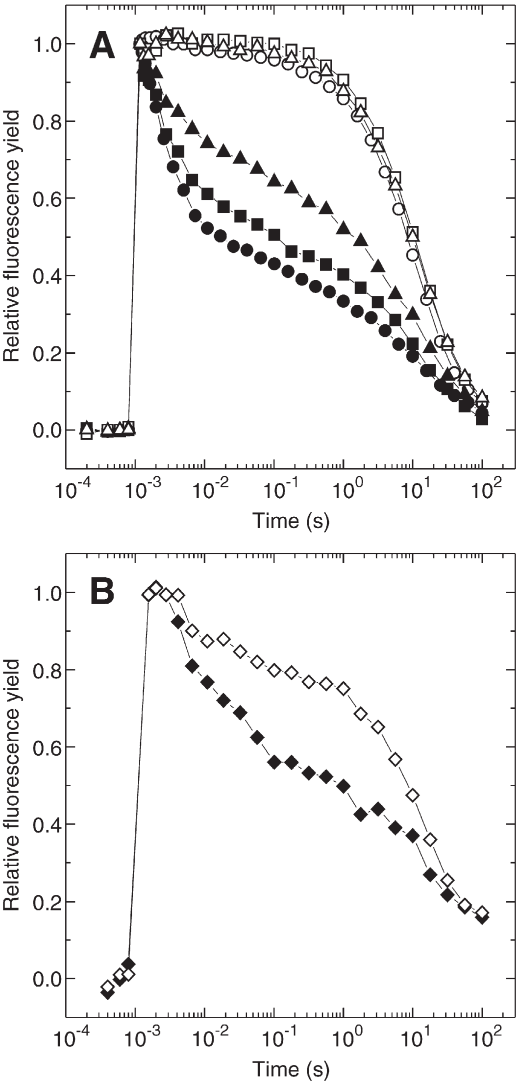

Fig. 5. Fluorescence relaxation kinetics in various PSII core preparations and in SrPSII crystals. (A) Flash-induced fluorescence decay from CaPSII and SrPSII core dimers. 100% Ca^{2+} (circles), 50% Sr^{2+} (squares), 100% Sr^{2+} (triangles) in Mn_4Ca cluster of the OEC. (B) Fluorescence relaxation kinetics in SrPSII crystals obtained from *T. elongatus* core preparations with 50% Sr^{2+} occupancy in the Mn_4Ca cluster of the OEC (diamonds). Relaxation of the flash-induced chlorophyll fluorescence yield was measured in the absence (closed symbols) or in the presence of 10 μM DCMU (open symbols). The traces of the PSII cores represent the average of 5 (CaPSII) and 3 (SrPSII) curves. The curves obtained from SrPSII crystals represent the average of 20 traces. All traces are normalised to the same initial amplitude.

for that in the absence of the inhibitor, efficient reoxidation of Q_A occurs via electron transfer in centres containing bound PQ at the Q_B site.

3.4. Identification of strontium electron density in the SrPSII crystals

A feature of the OEC of PSII is that the Mn ions and Ca^{2+} are in close proximity to each other and therefore, high-resolution structural information is required to resolve them as individual metal ions. The PSII crystals are characterised by a large unit cell, weak X-ray diffraction, and susceptibility to radiation damage, including photoreduction of Mn in its high valency states [19]. The K-absorption edge of Ca^{2+} is at 4.03 keV (3.07 Å), a wavelength that is technically difficult to access at synchrotrons. The main reason for replacing Ca^{2+} with Sr^{2+} was to gain a better insight into the geometry of the OEC metals, a strategy which has been previously adopted for EXAFS analyses [13]. Strontium has a K-absorption edge at 16.1 keV (0.7699 Å), which is accessible at MAD beamlines. As a result, we have been able to collect and analyse X-ray diffraction data generated by the SrPSII crystals and identified a novel Sr^{2+} site shown in Fig. 6.

Two full datasets were collected from different regions of the same SrPSII crystal, above and below the Sr K-edge, dubbed Sr-HER and Sr-LER (see Fig. 6A, B). The Sr-HER and Sr-LER datasets were processed to 6.5 Å (see Suppl. Table S1), since the resolution was limited by radiation damage. The top 11 peaks in the Sr-LER-DANO map corresponded to sulphur or iron atoms, except peak 8 (0.39 of the height of the top peak shown as green mesh in Fig. 6), which was at the OEC site. The strongest peak not associated with an atom with an atomic number less than sulphur was 0.22 of the top peak and represents the magnitude of the background noise. The top 9 peaks in the Sr-HER-DANO map corresponded to sulphur atoms, except peak 6 (0.71 of the height of the highest peak) which corresponded to the OEC (shown as blue mesh in Fig. 6). The strongest noise peak was 0.27 of the height of the top peak. The first noise peak was 0.27 the height of the top peak. For the Sr-DDANO map, the top peak was at the OEC site (shown as red mesh in Fig. 6), and subsequent peaks corresponded to noise with the strongest being 0.64 of the height of the top peak. The peaks at the OEC for the 3 maps are named Sr-LER-OEC, Sr-HER-OEC and Sr-DDANO-OEC. DDANO-OEC is 1.65 Å and 1.88 Å away from the Ca^{2+} ions of the 1S5L.pdb [17] and 2AXT.pdb [18] models of the OEC, respectively (see Suppl. Table S2). This is closer to the Ca^{2+} than any of the Mn atoms in either OEC model, of which the closest distance is 2.6 Å (see Suppl. Table S2). The DDANO-OEC site is only a little further from the Ca^{2+} ions of the two models than they are from each other (1.12 Å, see Suppl. Table S2). This Sr^{2+} electron density is clearly resolvable from the adjacent atoms of the Mn cluster and, within the resolution of the data, is consistent with the proposed position of Ca^{2+} in the OEC [17,18].

4. Discussion

Following the example of Boussac et al. [11], we have grown the thermophillic cyanobacterium *T. elongatus* in a medium having Sr^{2+} replacing Ca^{2+}. In this way PSII preparations were

Table 1
Comparison of crystallized SrPSII and CaPSII activities measured by fluorescence imaging

Crystal type	F'_0	F_m	F_v/F_m	% F_v/F_m
SrPSII (100% Sr^{2+})	0.046 ± 0.004	0.080 ± 0.003	0.434 ± 0.038	74.8
SrPSII (50% Sr^{2+})	0.051 ± 0.004	0.100 ± 0.004	0.490 ± 0.036	84.6
CaPSII	0.046 ± 0.005	0.110 ± 0.013	0.580 ± 0.059	100

Values represent average measurements obtained from 20 to 30 crystals.

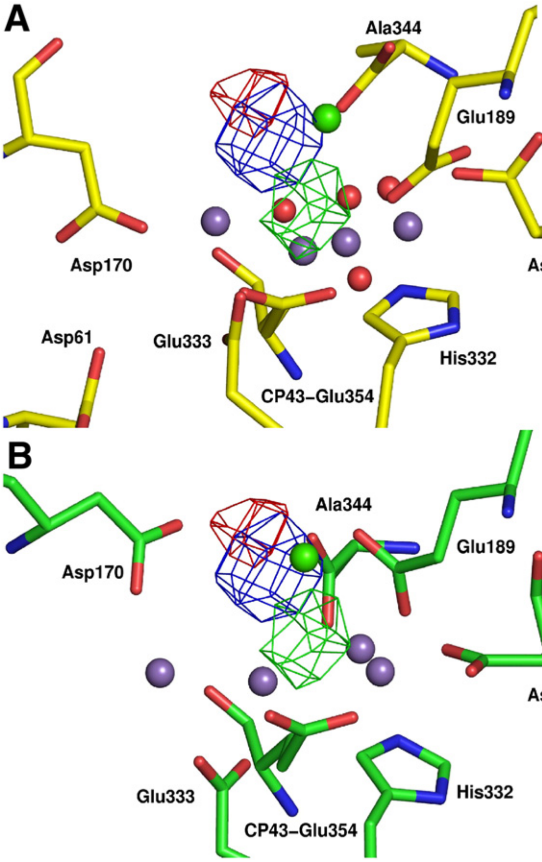

Fig. 6. Anomalous difference electron density maps for the Sr-LER dataset (green), contoured at 12 sigma, and Sr-HER dataset (blue) at 18 sigma and the Sr-DDANO double anomalous difference density (red) at 12 sigma. The double difference peak is closer to the calcium atom (green ball) of the PSII crystallographic models 1S5L.pdb [17] (depicted in A) and 2AXT.pdb [18] (shown in B) than any of the manganese atoms (purple balls). The oxygen atoms modelled in 1S5L.pdb [17] are shown as red balls. Two datasets were collected from different regions of the same crystal, above and below the Sr K-edge, dubbed HER and LER. The HER and LER datasets were collected as described in Materials and methods.

isolated with complete or partial replacement of Ca^{2+} by Sr^{2+} in the OEC. Oxygen evolution rates and chlorophyll fluorescence measurements gave results which were consistent with modifications to the kinetics of the S-state cycle when Sr^{2+} replaces Ca^{2+}, as concluded for the cyanobacterial SrPSII [11] and for the higher plant counterpart [4,44,45]. Here we found that this effect was manifested by a slowing down of electron transfer between Q_A and Q_B and as stabilization of the $S_2Q_A^-$ charge transfer state. For the first time, we were successful in growing 3D crystals of PSII with complete or approximately 50% replacement of Ca^{2+} with Sr^{2+}. The results of chlorophyll fluorescence measurements conducted on both types of SrPSII crystals indicted that they were functionally active with characteristic consistent with soluble SrPSII complexes. The differences between native CaPSII and SrPSII at the level of their electron transport kinetics may correlate with structural and mechanistic changes of the catalytic metal cluster. Boussac et al. [11] have shown that substitution of Ca^{2+} by Sr^{2+} in the OEC leads to stabilization of the S_3-state, increased rate of oxidation of the S_0 to S_1-state by Tyr_D and the slowdown of the S_3Tyr_Z to S_0Tyr_Z transition. Recently, FT-IR studies [46,47] provided further evidence of perturbation of hydrogen bond network involving Ca^{2+}, water molecules and peptide carbonyl groups of ligands to Mn ions of the OEC during S-state transitions upon Sr^{2+} substitution.

The purpose of replacing Ca^{2+} with Sr^{2+} in the OEC was to take advantage of the accessibility to its X-ray absorption edge so as to collect anomalous diffraction data and calculate difference maps. A similar reasoning has been made for investigating the positioning of Ca^{2+} in the OEC using EXAFS [12,13]. These earlier studies involved in vitro biochemical replacement of Ca^{2+} by Sr^{2+}, indicated that Sr^{2+} was bound within 3.5 Å of the Mn-cluster. Complementary studies were undertaken later on untreated PSII containing Ca^{2+} in the OEC which gave credibility to the Sr^{2+} experiments and concluded that the Ca^{2+}–Mn distance was 3.4 Å [14].

At the time the work described here was started, no independent structural position of the Ca^{2+} site was available to confirm the assignment of Ferreira et al. [1]. Since then the 3.0 Å structure of Loll et al. has been published which placed Ca^{2+} of the OEC in about the same position as Ferreira et al., bearing mind the intermediate resolutions of both crystal structures [17,18]. The incorporation of Sr^{2+} gave us the opportunity to investigate further the binding position of Ca^{2+} and from our analyses this metal ion is clearly separated from the 4 Mn cations of the OEC site and consistent with the assignments in the published crystal structures [17,18]. Although it is now certain that Ca^{2+} is an intimate part of the OEC, its exact positioning relative to the 4 Mn ions and to the nearby protein environment will require an improvement in crystal quality and the adoption of procedures to alleviate the problem of radiation damage while collecting diffraction data. Nevertheless, the SrPSII crystals reported for the first time in this study provide invaluable material for complementary analysis of organisation of the OEC and its amino acid ligands using powerful techniques such as high-frequency EPR and ENDOR. It is hoped that these studies will allow for the determination of the precise arrangement of metal ions in the OEC and more importantly, correlate possible structural changes of the OEC with the functional S-state turnover of PSII.

Acknowledgements

JK, KM, JWM and JB are supported by the UK government Biotechnology and Biological Sciences Research Council (BBSRC). IV and ZD were supported by grants from EU (MRTN-CT-2003-505069, and STREP-SOLAR-H-516510). We are grateful to the staff of the Swiss Light Source facility, in particular Dr. Alke Meents, for their help and assistance during X-ray diffraction data acquisition. We thank Dr. Liz Carpenter (Imperial College London) for her advice with crystal harvesting and for helpful discussions.

Appendix A. Supplementary data

Supplementary data associated with this article can be found, in the online version, at doi:10.1016/j.bbabio.2007.01.007.

References

[1] J. Barber, Photosystem II: a multisubunit membrane protein that oxidises water, Curr. Opin. Struct. Biol. 12 (2002) 523–530.

[2] P. Joliot, G. Barbieri, R. Chabaud, Un nouveaux modele des centres photochimiques due systeme II, Photochem. Photobiol. 10 (1969) 309–329.

[3] B. Kok, B. Forbush, M. McGloin, Cooperation of charges in photosynthetic O_2 evolution, Photochem. Photobiol. 11 (1970) 457–475.

[4] A. Boussac, A.W. Rutherford, Nature of the inhibition of the oxygen-evolving enzyme of photosystem II induced by sodium chloride washing and reversed by the addition of calcium^{2+} or strontium^{2+}, Biochemistry 27 (1988) 3476–3483.

[5] C.F. Yocum, Calcium activation of photosynthetic water oxidation, Biochim. Biophys. Acta 1059 (1991) 1–15.

[6] R.J. Debus, The manganese and calcium ions of photosynthetic oxygen evolution, Biochim. Biophys. Acta 1102 (1992) 269–352.

[7] K.-C. Han, S. Katoh, Different localization of two Ca^{2+} in spinach oxygen-evolving photosystem II membranes. Evidence for involvement of only one Ca^{2+} in oxygen evolution, Plant Cell Physiol. 34 (1993) 585–593.

[8] T. Yamashita, G. Tomita, Light-reactivation of (Tris-washed)-DPIP-treated chloroplasts: manganese incorporation, chlorophyll fluorescence, action spectrum and oxygen evolution, Plant Cell Physiol. 17 (1976) 571–582.

[9] N. Tamura, Y. Inoue, G.M. Cheniae, Photoactivation of the water-oxidizing complex in photosystem II membranes depleted of Mn, Ca and extrinsic proteins. II. Studies on the functions of Ca^{2+}, Biochim. Biophys. Acta 976 (1989) 173–181.

[10] G.M. Ananyev, L. Zaltsman, C. Vasko, G.C. Dismukes, The inorganic biochemistry of photosynthetic oxygen evolution/water oxidation, Biochim. Biophys. Acta 1503 (2001) 52–68.

[11] A. Boussac, F. Rappaport, P. Carrier, J.-M. Verbavatz, R. Gobin, D. Kirilovsky, A.W. Rutherford, M. Sugiura, Biosynthetic Ca^{2+}/Sr^{2+} exchange in the Photosystem II oxygen evolving enzyme of *Thermosynechococcus elongatus*, J. Biol. Chem. 279 (2004) 22809–22819.

[12] M.J. Latimer, V.J. DeRose, I. Mukerji, V.K. Yachandra, K. Sauer, M.P. Klein, Evidence for the proximity of calcium to the manganese cluster of photosystem II: determination by X-ray absorption spectroscopy, Biochemistry 34 (1995) 10898–10909.

[13] R.M. Cinco, J.H. Robblee, A. Rompel, C. Fernandez, V.K. Yachandra, K. Sauer, M.P. Klein, Strontium EXAFS reveals the proximity of calcium to the manganese cluster of oxygen-evolving photosystem II, J. Phys. Chem., B 102 (1998) 8248–8256.

[14] R.M. Cinco, K.L. McFarlane Holman, J.H. Robblee, J. Yano, S.A. Pizarro, E. Bellacchio, K. Sauer, V.K. Yachandra, Calcium EXAFS establishes the Mn–Ca cluster in the oxygen-evolving complex of photosystem II, Biochemistry 41 (2002) 12928–12933.

[15] T.G. Carrell, A.M. Tyryshkin, G.C. Dismukes, An evaluation of structural models for the photosynthetic water-oxidizing complex derived from spectroscopic and X-ray diffraction signatures, J. Biol. Inorg. Chem. 7 (2002) 2–22.

[16] R.D. Britt, K.A. Campbell, J.M. Peloquin, M.L. Gilchrist, C.P. Aznar, M.M. Dicus, J. Robblee, J. Messinger, Recent pulsed EPR studies of the photosystem II oxygen-evolving complex: implications as to water oxidation mechanisms, Biochim. Biophys. Acta 1655 (2004) 158–171.

[17] K.N. Ferreira, T.M. Iverson, K. Maghlaoui, J. Barber, S. Iwata, Architecture of the photosynthetic oxygen-evolving center, Science 303 (2004) 1831–1838.

[18] B. Loll, J. Kern, W. Saenger, A. Zouni, J. Biesiadka, Towards complete cofactor arrangement in the 3.0 A resolution structure of photosystem II, Nature 438 (2005) 1040–1044.

[19] J. Yano, J. Kern, K.D. Irrgang, M.J. Latimer, U. Bergmann, P. Glatzel, Y. Pushkar, J. Biesiadka, B. Loll, K. Sauer, J. Messinger, A. Zouni, V.K. Yachandra, X-ray damage to the Mn4Ca complex in single crystals of photosystem II: a case study for metalloprotein crystallography, Proc. Natl. Acad. Sci. U.S.A. 102 (2005) 12047–12052.

[20] J.W. Murray, J. Barber, Identification of a calcium-binding site in the PsbO protein of photosystem II, Biochemistry 45 (2006) 4128–4130.

[21] M.E. Than, S. Henrich, G.P. Bourenkov, H.D. Bartunik, R. Huber, W. Bode, The endoproteinase furin contains two essential Ca^{2+} ions stabilizing its N-terminus and the unique S1 specificity pocket, Acta Crystallogr. D 61 (2005) 502–512.

[22] M. Sugiura, Y. Inoue, Highly purified thermo-stable oxygen-evolving photosystem II core complex from the thermophilic cyanobacterium *Synechococcus elongatus* having His-tagged CP43, Plant Cell Physiol. 40 (1999) 1219–1231.

[23] H. Schägger, G. von Jagow, Tricine-sodium dodecyl sulfate-polyacrylamide gel electrophoresis for the separation of proteins in the range from 1 to 100 kDa, Anal. Biochem. 166 (1987) 368–379.

[24] I. Vass, E. Turcsanyi, E. Touloupakis, D. Ghanotakis, V. Petrouleas, The mechanism of UV-A radiation-induced inhibition of photosystem II electron transport studied by EPR and chlorophyll fluorescence, Biochemistry 41 (2002) 10200–10208.

[25] A.G.W. Leslie, Recent changes to the MOSFLM package for processing film and image plate data. Joint CCP4+ESF-EAMCB Newsletter on Protein, Crystallography (1992) 26.

[26] P. Evans, Data reduction, CCP4 Daresbury Study Weekend DL/SCI R34 (1993) 114–122.

[27] A.J. McCoy, R.W. Grosse-Kunstleve, L.C. Storoni, R.J. Read, Likelihood-enhanced fast translation functions, Acta Crystallogr. D 61 (2005) 458–464.

[28] G.N. Murshudov, A.A. Vagin, E.J. Dodson, Refinement of macromolecular structures by the maximum-likelihood method, Acta Crystallogr. D 53 (1997) 240–255.

[29] The CCP4 Consortium, The CCP4 suite: programs for protein crystallography, Acta Crystallogr. D 50 (1994) 760–763.

[30] P.E. Stein, A. Boodhoo, G.D. Armstrong, S.A. Cockle, M.H. Klein, R.J. Read, The crystal structure of pertussis toxin, Structure 2 (1994) 45–57.

[31] W.L. DeLano, The PyMOL Molecular Graphics System, DeLano Scientific, San Carlos, CA, USA, 2002, http://www.pymol.org.

[32] E. Krissinel, K. Henrick, Secondary-structure matching (SSM), a new tool for fast protein structure alignment in three dimensions, Acta Crystallogr. D 60 (2004) 2256–2268.

[33] P. Emsley, K. Cowtan, Coot: model-building tools for molecular graphics, Acta Crystallogr. D 60 (2004) 2126–2132.

[34] D.F. Ghanotakis, G.T. Babcock, C.F. Yocum, Calcium reconstitutes high rates of oxygen evolution in polypeptide depleted photosystem II preparations, FEBS Lett. 167 (1984) 127–130.

[35] J.S. Vrettos, D.A. Stone, G.W. Brudvig, Quantifying the ion selectivity of the Ca^{2+} site in photosystem II: evidence for direct involvement of Ca^{2+} in O_2 formation, Biochemistry 40 (2001) 7937–7945.

[36] H. Kuhl, J. Kruip, A. Seidler, A. Krieger-Liszkay, M. Bunker, D. Bald, A.J. Scheidig, M. Rogner, Towards structural determination of the water-splitting enzyme. Purification, crystallization, and preliminary crystallographic studies of photosystem II from a thermophilic cyanobacterium, J. Biol. Chem. 275 (2000) 20652–20659.

[37] A. Boussac, M. Sugiura, Y. Inoue, A.W. Rutherford, EPR study of the oxygen evolving complex in His-tagged photosystem II from the cyanobacterium *Synechococcus elongatus*, Biochemistry 39 (2000) 13788–13799.

[38] A.R. Crofts, C.A. Wraight, The electrochemical domain of photosynthesis, Biochim. Biophys. Acta 726 (1983) 149–185.

[39] G. Renger, H.-J. Eckert, A. Bergmann, J. Bernarding, B. Liu, A. Napiwotzki, F. Reifarth, H.-J. Eichler, Fluorescence and spectroscopic studies of exciton trapping and electron transfer in photosystem II of higher plants, Aust. J. Plant Physiol. 22 (1995) 167–181.

[40] R. de Wijn, H.J. van Gorkom, Kinetics of electron transfer from Q_A to Q_B in photosystem II, Biochemistry 40 (2001) 11912–11922.

[41] W. Oettmeier, Herbicide resistance and supersensitivity in photosystem II, Cell. Mol. Life Sci. 55 (1999) 1255–1277.

[42] I. Vass, S. Styring, T. Hundal, A. Koivuniemi, E. Aro, B. Andersson, Reversible and irreversible intermediates during photoinhibition of photosystem II: stable reduced QA species promote chlorophyll triplet formation, Proc. Natl. Acad. Sci. U.S.A. 89 (1992) 1408–1412.

[43] K. Zimmermann, M. Heck, J. Frank, J. Kern, I. Vass, A. Zouni, Herbicide binding and thermal stability of photosystem II isolated from *Thermosynechococcus elongatus*, Biochim. Biophys. Acta 1757 (2006) 106–114.

[44] A. Boussac, P. Sétif, A.W. Rutherford, Inhibition of tyrosine Z photooxidation after formation of the S_3 state in Ca^{2+}-depleted and Cl^{-} depleted photosystem II, Biochemistry 31 (1992) 1224–1234.

[45] K.L. Westphal, N. Lydakis-Simantiris, R.I. Cukier, G.T. Babcock, Effects of Sr^{2+}-substitution on the reduction rates of Yz* in PSII membranes-evidence for concerted hydrogen-atom transfer in oxygen evolution, Biochemistry 39 (2000) 16220–16229.

[46] M.A. Strickler, L.M. Walker, W. Hillier, R.J. Debus, Evidence from biosynthetically incorporated strontium and FTIR difference spectroscopy that the C-terminus of the D1 polypeptide of photosystem II does not ligate calcium, Biochemistry 44 (2005) 8571–8577.

[47] H. Suzuki, Y. Taguchi, M. Sugiura, A. Boussac, T. Noguchi, Structural perturbation of the carboxylate ligands to the Mn cluster upon Ca^{2+}/Sr^{2+} exchange in the S-state cycle of photosynthetic oxygen evolution as studied by flash-induced FTIR difference spectroscopy, Biochemistry 45 (2006) 13454–13464.